High temperature corrosion during biomass firing: improved understanding by depth resolved characterisation of corrosion products

Okoro, Sunday Chukwudi; Montgomery, Melanie; Jappe Frandsen, Flemming; Pantleon, Karen

Published in:
Materials at High Temperatures

Link to article, DOI:
10.1179/0960340914Z.00000000081

Publication date:
2015

Document Version
Peer reviewed version

High Temperature Corrosion during Biomass Firing: Improved Understanding by Depth-Resolved Characterization of Corrosion Products

Sunday Chukwudi Okoro[1,*], *Melanie Montgomery*[1,3], *Flemming Jappe Frandsen*[2], *Karen Pantleon*[1]

[1]*Technical University of Denmark (DTU), Department of Mechanical Engineering, Building 425, 2800 Kongens Lyngby, Denmark.*

[2]*DTU, Department of Chemical and Biochemical Engineering, Building 228, 2800 Kongens Lyngby, Denmark.*

[3]*COWI A/S, Parallelvej 2, 2800 Kongens Lyngby, Denmark*

* Phone: +45 50185680, Fax: +45 45936213, Email: sunoko@mek.dtu.dk, okorochukwudi@ymail.com

Abstract: The high temperature corrosion of an austenitic stainless steel (TP 347H FG), widely utilised as a superheater tube material in Danish power stations, was investigated to verify the corrosion mechanisms related to biomass firing. KCl coated samples were exposed isothermally to 560 ^{o}C, for one week, under conditions simulating straw-firing. Thorough characterisation of the exposed samples was conducted by the analysis of sample cross sections applying microscopy and spectroscopy based techniques. Cross section analysis revealed the microstructure, as well as chemical and morphological changes within the near surface region (covering both the deposit and the steel surface). Such cross section analysis was further complemented by plan view investigations (additionally involving X-ray diffraction) combined with removal of the corrosion products. Improved insights into the nature of the corrosion products as a function of distance from the deposit surface were revealed through this comprehensive characterization. Corrosion attack during simulated

straw-firing conditions was observed to occur through both active oxidation and sulphidation mechanisms.

Keywords: Fireside corrosion, active oxidation, sulphidation, KCl deposit

1 Introduction

There is a growing interest in Scandinavia for converting thermal power plants initially firing fossil fuels to biomass firing (in Denmark, usually straw). The major motivation for such fuel substitution is reducing the CO_2 emissions in the atmosphere.[1] Biomass is able to recapture the CO_2 emitted during combustion in a shorter time, relative to fossil fuels. Additionally, the availability of biomass makes it a worthwhile energy source.[1,2] However, the chemical composition of biomass is different from that of fossil fuels. As such, several operational challenges are experienced in power plants firing biomass. One of such challenges is related to condensation of aerosol and fly ash particles rich in KCl and K_2SO_4, leading to fast corrosion rates of the superheater tubes. [3–5] To limit corrosion, the outlet steam temperatures in Danish biomass power plants are kept below 540 ^oC (corresponding to a metal temperature of 560 ^oC).[6] This compromises the efficiency of the power plants firing biomass relative to those firing fossil fuels. To overcome these challenges, it is necessary to fully understand the mechanisms involved in the corrosion of superheater tubes during biomass firing. Information from such studies would guide the development of advanced materials with properties to withstand the corrosivity of biomass.

Several reports in the literature have helped to understand the mechanism of corrosion under a synthetic deposit (KCl, NaCl, $CaCl_2$, etc.), HCl, or H_2O vapour.[7–14] In such corrosive atmospheres, the observed corrosion is mostly accepted to proceed according to the active oxidation mechanism, sustained by Cl.[15,16] However, the operating conditions, as well as the

corrosive atmosphere in a biomass power plant are complex, and accordingly, studies under laboratory conditions are often simplified. A few studies [1,15,17–19] have investigated both the influence of the flue gas, and the synthetic deposit during laboratory exposure, in order to generate more realistic information regarding the corrosion mechanisms. Under such complex conditions, however, complete characterization of the resulting corrosion products is challenging if solely based on conventional metallographic techniques, and thus, not fully explored yet.

This paper reports the results from a comprehensive characterization of corrosion products, resulting from high temperature corrosion studies of an austenitic stainless steel (TP 347H FG) under laboratory conditions simulating straw-firing. Both conventional cross section characterization, and a plan view, 'top-down', characterization approaches were employed and these complemented each other in improving understanding of the corrosion products formed as a function of distance from the deposit surface

2 Experimental Procedure

2.1 Sample preparation, deposition and high temperature exposure

An unexposed austenitic stainless steel tube with a fine grained microstructure (TP 347H FG) was investigated (Table 1 gives the chemical composition). The tubes were first cut into rings with a width of 1 cm. These were then sectioned into arc shaped samples. Before coating with synthetic deposits, the cut samples were degreased in acetone and ethanol using an ultrasonic bath.

Table 1 Chemical composition (in wt-%) determined by Energy-dispersive X-ray Spectroscopy (EDS), of the as-received austenitic stainless steel (TP 347H FG) investigated.

Si	Cr	Mn	Ni	Fe	Nb
0.4	18.1	2.0	10.3	68.7	0.5

An approach similar to the 'deposit recoat' method was employed in order to maintain the EU guidelines for effective testing of deposit induced fireside corrosion. [20,21] Pure KCl particles with particle size ranging from 32-60 µm were used as a synthetic deposit. These particles were mixed with a solution of isopropyl alcohol to give a slurry of the deposit. The concave side of the cut samples were then uniformly coated with about 5.21 mg cm^{-2} (on a solvent free basis) of the deposit slurry.

High temperature exposure of the samples was carried out at 560 ^{o}C for 168 h. To this end, a dedicated corrosion test setup was used for simulating straw-firing, although on a laboratory scale (cf. Fig. 1).

In the setup, an electrically heated furnace containing five quartz reactors allows for five simultaneous experimental runs. A sample was exposed in each reactor. A well-defined gas mixture corresponding to the flue gas composition during straw firing was simulated using mixtures of HCl, SO_2, CO_2 and O_2, as given in Table 2. The gaseous mixture of N_2, CO_2 and O_2 was passed through a humidifier to incorporate H_2O. Finally, the humid gas mixture was mixed with HCl and SO_2 prior to feeding into the reactors. N_2 was utilized as a carrier gas. Mass flow regulators were employed to maintain the desired concentration of the gases, while a ball flow meter was connected to the exit of each reactor in order to maintain a uniform gas flow in each reactor.

Table 2 Dry flue gas composition used to simulate straw firing conditions

Gas	HCl	SO_2	O_2	CO_2	N_2
Concentration	400 ppmv	60 ppmv	6 vol.-%	12 vol.-%	82 vol.-%

2.2 Materials Characterization

Microscopic analysis by scanning electron microscopy (SEM), EDS and X-ray diffraction (XRD) were employed to fully characterize the microstructure including the chemical and phase composition of the resulting corrosion products on the exposed samples. Two characterization approaches were employed: cross-sectional characterization of the samples, as well as a plan view 'top-down' characterization, availed by removal of the corrosion products.

Prior to cross-sectional investigations, an exposed sample was mounted in epoxy under vacuum, to preserve the morphologies of the corrosion products during further sample handling. Subsequently, the embedded sample was cut along the long axis and embedded again in epoxy, this time to access the sample cross section. Afterwards, water-free metallographic preparation of the sample cross sections was carried out.

The plan view 'top-down' characterization combined with corrosion product removal was carried out on an exposed sample without embedding in epoxy or metallographic preparation. For removal of the corrosion products either a scalpel or gentle grinding with silicon carbide (SiC) was used. Before and after each removal, characterization by SEM, EDS and XRD was carried out.

FEI (Inspect S) and JEOL (JSM 5900) SEM operated at 15 kV were used for SEM investigations. An Oxford Inca and Aztec EDS system attached to the SEM was employed for

chemical element analysis. For XRD characterization, a Bruker AXS diffractometer (Discover D8) was used with Cr-Kα radiation in grazing incidence geometry at an X-ray incidence angle of 3° and 5° (for direct measurements on the deposit).

Fig. 2a presents a schematic illustration of this depth-resolved characterization approach. A more detailed description of a similar approach is reported elsewhere.[22]

3 Results

3.1 Investigations of the cross section

The results presented here are representative of the samples exposed in the five reactors. Three layers of corrosion products were identified from cross-sectional characterization of the exposed sample (Figs. 2b and 3). The topmost layer, Layer 1-cs (cross section), located directly below the initial deposit is observed to contain bright pin-shaped features in a darker matrix. The average thickness of this layer, apparently consisting of at least two phases, amounts to about 31.3 ± 6.8 µm. The second layer, Layer 2-cs contains some porosity which becomes severe at the interface between Layer 1-cs and Layer 2-cs. For Layer 2-cs, an average thickness of about 18.5 ± 7.8 µm was determined. It appears that both Layer 1-cs and Layer 2-cs are formed below the original deposit, whereas Layer 3-cs is formed above the corrosion front, directly below Layer 2-cs. This Layer 3-cs of the corrosion product is observed to be very porous with a sponge-like morphology covering a thickness of about 10.8 ± 2.6 µm.

Fig. 3 presents the EDS elemental maps from analysis carried out on a cross section of the exposed sample. The elemental maps show that the topmost corrosion product (Layer 1-cs) consists mainly of potassium (K), sulphur (S), oxygen (O) and iron (Fe). The layer below, i.e. Layer 2-cs, is observed to contain chromium (Cr), Fe and O. The Cr map shows that the

element is more concentrated in the lower parts of Layer 2. Close to the steel surface, Layer 3-cs, a strong band is observed in the nickel (Ni) map. Additionally, at the same location of increased Ni content, increased concentrations of S were detected, suggesting that Layer 3 of the corrosion product contains predominantly Ni and S.

3.2 Plan view 'top-down' characterization

The microstructure of the synthetic KCl deposit after the exposure, as observed from plan view investigations is presented in Fig. 4. It is pertinent to mention that the Cl containing epoxy embedding causes some technical challenges during cross-sectional characterization of the initial deposit. The Cl from the embedding matrix usually overlaps with Cl peaks from the deposit during EDS analysis. Additionally, some deposits become detached from the epoxy matrix during metallographic preparation, and in some cases, Si and Mg from the grinding and polishing process accumulate on these free spaces. Such technical difficulties posed by the epoxy embedding towards proper characterization of the initial deposit during cross-sectional investigations were overcome through the plan view top-down characterization approach on the non-embedded sample. The micrograph in Fig. 4a shows the structure of the deposit particles observed at the FG/DP interface (i.e. location (i) in Fig. 2a).

An interesting and noteworthy observation is the accumulation of apparently party 'molten' particle clusters around the deposit particles. A similar observation is seen from the micrograph (Fig. 4b) obtained at the DP/ CP interface (position (ii) in Fig. 2a). However, the sizes of the clusters in Fig. 4b are relatively smaller, probably because of the limited availability of SO_2 at the DP/CP interface. In addition, light particles are seen on these clusters at this location. Based on the grayscale level, it is not possible to conclude whether these light particles are also present on the initial deposit particles. EDS analysis on the partly 'molten' particle clusters indicated the presence of K, S, and O. The identification of S on

these particles suggests that the initial synthetic deposit has been sulphated during the high temperature exposure due to the presence of SO_2 in the simulated flue gas. In addition, at the DP/CP interface, the presence of minor amounts of Fe was also observed by EDS analysis.

XRD measurements on exposed samples, both at the FG/DP interface and DP/CP interface are presented in Fig. 5. Crystalline phases which could be identified by XRD at these locations correspond to KCl and K_2SO_4. This observation also supports results from EDS analysis, thereby confirming the formation of K_2SO_4 due to sulphation of the initial deposit particles during the high temperature exposure.

Removal of the initial deposit using a scalpel revealed the presence of three layers of corrosion products (Fig. 6). The surface removal did not yield a flat even surface but three layers of different morphology became visible. This could be due to the inhomogeneous nature of the corrosion products as already seen in Fig. 3. These three layers were thoroughly characterized by SEM and EDS from the directions indicated as (iii), (iv), (v) and (vii) in Fig. 2a.

SEM images of the first layer of corrosion product (Layer 1-pv (plan view)) are presented in Fig. 7. The micrographs reveal the presence of dark particle clusters on a porous partly ‘molten’ layer. The contrast observed in these BSE micrographs suggests a difference in chemical composition. EDS analysis of the darker particle clusters showed that the layer is composed mainly of O, S and K with minor amounts of Fe and Cl. Conversely, EDS analysis of the brighter, partly ‘molten’ layer showed the presence of Cl, K and Fe. Minor amounts of S and Mn were also identified in this partly ‘molten’ layer. Since the contrast in BSE images depends on the atomic number of elements (brighter regions correspond to higher atomic number), the light particles observed on the partly ‘molten’ layer are expected to be rich in Fe (see also the discussion below).

In Fig. 8, plan view micrographs from Layer 2-pv (Fig. 6) of the corrosion product are presented. The micrographs, Figs. 8a, 8b and 8c were obtained from investigations in the direction indicated as (iv) in Fig. 2a. Three major morphological features observed on Layer 2-pv were revealed:

a) Features of well-defined geometry with mainly two-fold symmetry (Fig. 8a). These were identified by EDS to contain significant amounts of Fe (68.4 wt.-%) and oxygen, as well as minor amounts of Mn and Cr (< 4 wt.-%). Very low amounts of K and Cl were also identified within these features.

b) Hollow shaped structures arranged in a zigzag pattern (Fig. 8b). In-between these features, some of the features observed in (a) are also present. The BSE image shows no contrast between the two-fold symmetric features embedded in these hollow structures and the hollow shaped Zigzag pattern, thereby suggesting a similar composition for both features. Interestingly, EDS investigations showed that these areas also contain significant amounts of Fe (53.3 wt.-%) and oxygen, also with minor amounts of Mn. However, the amount of Cr (13.3 wt.-%) identified in these regions was higher than that within the features in Fig. 8a. Similarly, low amounts of K and Cl were also identified.

c) Whiskers on coral-like structures (Fig. 8c). Faceted particles are also observed within these features. These faceted particles are arranged in coral-like structures with very thin whiskers. Analysis by EDS revealed an increased amount of K and Cl within these features (~9 wt.-%) relative to that observed within the previously described features (in Fig. 8a and 8b). The Fe, Mn and Cr amounts identified within this feature, were within the range observed in the previously described features in (a) and (b).

Microscopic investigations of Layer 2-pv, from the CP/ST interface (position (vi) in Fig. 2a) are shown in Fig. 8d. A continuous porous and buckled layer containing some features of well-defined geometry (similar to the ones in Fig. 8a, but much larger) can be observed. These features were identified through EDS analysis to contain about 68.9 wt.-% of Fe and 27.6 wt.-% of O, in addition to minor amounts of Cr, Mn and Ni. In contrast, the porous and buckled layer contained a lower amount of Fe (29.6 wt.-%), but, a higher amount of Cr (37.1 wt.-%). Si, S, Cl, K and Ni were also identified in this porous layer (see Fig. 8d). In general, the chemical composition of Layer 2-pv correspond to that observed in Layer 2-sc (Figs. 2b and 3), however, from plan view top-down characterization, more detailed information regarding the morphology and distribution of elements in this layer is achieved.

XRD analysis on Layer 2-pv, i.e. the CP/ST interface is included in Fig. 5 (position (vi) refers to this location). Crystalline phases which could be identified by XRD include chromite ($FeCr_2O_4$), hematite (Fe_2O_3), potassium sulphate (K_2SO_4) and potassium chloride (KCl).

The micrographs in Fig. 9 present the change in microstructure of Layer 3-pv of the corrosion product (position (viii) in Fig. 2), as the corrosion front is approached. The brighter regions in Fig. 9a correspond to the bulk alloy. EDS analysis from a plan view on the porous (dark) region in Fig. 9a revealed a very high Ni concentration (27.3 wt.-%), as well as the presence of S (5 wt.-%), with minor amounts of Cl and K. Other alloying elements (Cr, Fe and Ni) were detected within this porous region. Oxygen was intentionally not considered in the ESD analysis because of the uncertainty with elements of lower atomic numbers during EDS analysis. It is important to point out that the porous nature of Layer 3-sc, as well as the possibility of generating BSE from an obscured interaction volume below the observed layer, might influence results of the EDS maps in Fig. 4. However, the consistent identification of high Ni concentration and S, from the plan view EDS analysis within this porous region (Fig.

10) authenticates that the S band is located in similar points with Ni, as observed in EDS elemental maps across the sample cross section (Fig. 4).

In Fig. 9a, isolated dark protrusions rich in chlorine are revealed within the porous region. The morphology of the Cl-rich protrusions suggests that they have been molten. EDS analysis shows an average Cl concentration of 30.4 wt.-% in these melt phases. Oxygen was deliberately eliminated during the EDS analysis in order to carefully track the change in concentration of other elements. Interestingly, the amount of K present in these phases (1.4 wt.-%), is insufficient to chemically balance both S and Cl anions. Relative to other cations, only an increase in Ni concentration is observed within the melt phases (32.5 wt.-% compared to 27.3 wt.-% in the porous region). Other cations exhibited a decrease in concentration in these melt phases, thereby suggesting that the Cl is probably associated with Ni. These observations are also evident in the EDS elemental maps showing the distribution of elements on this location (Fig. 10). With further progress towards the corrosion front (Fig. 9b), the local attack occurs along the grain boundaries, due to the faster diffusion pathway provided by grain boundaries relative to the grain interiors.

Results from XRD measurements (location (vii) in Fig. 2a) showed the presence of $FeCr_2O_4$ and Fe_2O_3 within the porous layer of corrosion product. The intensity of peaks corresponding to these phases decreases and finally disappears as the bulk is approached. Additionally, diffraction from Ni_3S_2 is also recorded in the diffractogram. In contrast to the peaks of $FeCr_2O_4$ and Fe_2O_3, these peaks showed increased intensity before disappearing as the bulk of the steel is approached. This implies that the Ni_3S_2 phase becomes dominant at certain depths probably within the porous layer (Layer 3) of the corrosion product.

4 Discussion

The results of the present work show similarity to those observed from the corrosion of superheater tubes in boilers firing straw.[23–25] The initial synthetic KCl deposit was observed to have partly sulphated during exposure to laboratory conditions simulating straw-firing at 560 ºC. The sulphation of KCl proceeds through an adsorption mechanism, and is expected to produce either HCl or Cl depending on the exposure conditions. [26,27] Under humid conditions, the sulphation is expected to proceed according to equation (1). This will explain the S-rich partly 'molten' particle clusters observed around the initial KCl deposit particles (Fig. 6), as well as the K and S rich layer in Fig. 3. The HCl resulting from the sulphation reaction, can be oxidized to generate molecular chlorine (equation 2) which is able to diffuse easily, to the corrosion front through imperfections or via an electrochemical route.[12,28,29]

$$2\mathrm{KCl(s)} + \mathrm{SO_2(g)} + \frac{1}{2}\mathrm{O_2(g)} + \mathrm{H_2O} \rightleftharpoons \mathrm{K_2SO_4(s)} + 2\mathrm{HCl(g)} \qquad (1)$$

$$2\mathrm{HCl(g)} + \frac{1}{2}\mathrm{O_2(g)} \rightleftharpoons \mathrm{Cl_2(g)} + \mathrm{H_2O(g)} \qquad (2)$$

Alternatively, in the presence of an initial Cr_2O_3 layer, it is expected that the KCl deposit can react with the oxide to form potassium chromate and thereby diminish the Cr content near the surface regions. Subsequent formation of an unprotective Fe-rich oxide ensues.[30,31] The Cl generated from such a reaction can also diffuse through the unprotective oxide towards the oxide/alloy interface.

At the oxide layer/alloy interface the conditions are reducing. At this location, Cl is thermodynamically able to react with metal alloying elements to produce metal chlorides (equation 3). The thermodynamics of such reactions are discussed in detail in the literature [28,32].

$$M(s) + xCl \rightleftharpoons MCl_x(s) \qquad (3)$$

Due to their volatility, these metal chlorides are able to diffuse towards the oxide/flue gas interface. However, the rate of vaporization of these metal chlorides is element dependent. The identification of Ni-rich chloride melt phases close to the bulk alloy shows that Cr- and Fe-chloride vaporization occurs faster than that of Ni-chloride. This observation is in agreement with thermodynamic calculations discussed in the literature.[28,32–34] The evaporating metal chlorides, experience a higher oxygen potential, as they approach the oxide/flue gas interface and thus will form metal oxides.

The chloride released from this oxidation can diffuse back to the oxide/steel interface (corrosion front) through the unprotective oxide. Such a cyclic corrosion mechanism caused by Cl is termed the 'chlorine cycle' and is chiefly responsible for the active oxidation of steels in Cl-containing environments.[33,35] Following such a mechanism, the likely oxides to be observed in a Fe-Cr-Ni alloyed steel (similar to the alloy investigated in the present work) are the Fe and Cr oxides. This is because the alloying elements, Fe and Cr have a higher affinity for Cl(to generate metal chlorides), relative to that of Ni . Similarly, the metal chlorides of Fe and Cr require lower oxygen potentials for oxidation relative to that of Ni . .[28] Through the top-down characterization approach, Fe and Cr rich O-containing layers of corrosion products were observed below the initial deposit. This was verified by XRD characterization to correspond to $FeCr_2O_4$ and Fe_2O_3. Results shown in Fig. 8c also show the presence of coral-like Cl-rich whiskers. The chlorine observed at these locations could have resulted from the oxidation of the metal chlorides as they approach regions with higher oxygen potentials.

A common observation from both cross-sectional and plan view 'top-down' characterization is the occurrence of a porous Ni-rich layer very close to the bulk alloy. The

thermodynamically favoured reaction of Cl with Fe and Cr is also responsible for the selective nature of attack, thereby leaving behind a porous Ni matrix. However, it is noticed that S is able to migrate through the porous oxide layer to these regions of selective attack. Despite the possible technical challenges in obtaining precise chemical information from the porous layer of corrosion product, the plan view EDS analysis validated the presence of S together with Ni within this porous layer. The EDS analysis was correlated with XRD measurements to show the presence of Ni_3S_2in this porous layer. As Ni is the most abundant element in such locations, the formation of nickel sulphide clearly indicates sulphidation.

5 Conclusions

Thorough characterization of corrosion products on an austenitic stainless steel exposed to straw-firing conditions in a laboratory have been carried out.

- By complementary use of microscopic (SEM), spectroscopic (EDS) and diffraction (XRD) based techniques, an improved identification of corrosion products resulting from simulated straw-firing conditions is achieved.

- Through a combination of cross-sectional and plan view ‘top-down’ characterization approaches, the identified crystalline corrosion products from the three layers were: K_2SO_4 and KCl (Layer 1), $FeCr_2O_4$ and Fe_2O_3 (Layer 2), and Ni_3S_2 (Layer 3).

- By the use of a plan view top-down characterization method, it was possible to reveal site specific information, such as the sulphation of the initial deposit, the formation of a partly ‘molten’ KCl layer below the deposit, and the formation of Ni-Cl melt phases as well as a Ni_3S_2 phase in the corrosion products close to the corrosion front.

- These observations suggest that the corrosion mechanisms under laboratory conditions simulating straw-firing involves both active oxidation (chlorination) and sulphidation.

Acknowledgement

This work is part of the Danish Strategic research center ‘Power Generation from Renewable Energy’ (GREEN). The authors acknowledge funding by the Danish Council for Strategic Research.

References

1. F. J. Frandsen: '*Ash Formation , Deposition and Corrosion when Utilizing Straw for Heat and Power Production*', Doctoral thesis, Technical Univeristy of Denmark, Kongens Lyngby, Denmark, 2011,1–341.

2. H. P. Nielsen, F. J. Frandsen, K. Dam-Johansen, and L. L. Baxter, 'The implications of chlorine-associated corrosion on the operation of biomass-fired boilers,' *Prog. Energy Combust. Sci.*, 2000, **26**, 283–298.

3. K. A. Christensen, M. Stenholm, and H. Livbjerg, 'The formation of submicron aerosol particles, HCl and SO_2 in straw-fired boilers,' *J. Aerosol Sci.*, 1998, **29**, 421–444.

4. H. P. Michelsen, F. Frandsen, K. Dam-Johansen, and O. H. Larsen, 'Deposition and high temperature corrosion in a 10 MW straw fired boiler,' *Fuel Process. Technol.*, 1998, **54**,95–108.

5. P. A. Jensen, M. Stenholm, and P. Hald, 'Deposition Investigation in Straw-Fired Boilers,' *Energy & Fuels*, 1997, **11**,1048–1055.

6. M. Montgomery, S. A. Jensen, U. Borg, O. Biede, and T. Vilhelmsen, 'Experiences with high temperature corrosion at straw-firing power plants in Denmark,' *Mater. Corros.*, 2011, **62**, 593–605.

7. J. Pettersson, J.-E. Svensson, and L.-G. Johansson, 'KCl-Induced Corrosion of a 304-type Austenitic Stainless Steel in O_2 and in $O_2 + H_2O$ Environment: The Influence of Temperature,' *Oxid. Met.*, 2009, **72**, 159–177.

8. Y. S. Li, M. Spiegel, and S. Shimada, 'Corrosion behaviour of various model alloys with NaCl–KCl coating,' *Mater. Chem. Phys.*, 2005, **93**, 217–223.

9. S. Enestam, D. Bankiewicz, J. Tuiremo, K. Mäkelä, and M. Hupa, 'Are NaCl and KCl equally corrosive on superheater materials of steam boilers?,' *Fuel*, 2013, **104**, 294–306.

10. S. Karlsson, J. Pettersson, L.-G. Johansson, and J.-E. Svensson, 'Alkali Induced High Temperature Corrosion of Stainless Steel: The Influence of NaCl, KCl and $CaCl_2$,' *Oxid. Met.*, 2012, **78**, 83–102.

11. J. Lehmusto, B.-J. Skrifvars, P. Yrjas, and M. Hupa, 'High temperature oxidation of metallic chromium exposed to eight different metal chlorides,' *Corros. Sci.*, 2011, **53**, 3315–3323.

12. N. Folkeson, L.-G. Johansson, and J.-E. Svensson, 'Initial Stages of the HCl-Induced High-Temperature Corrosion of Alloy 310,' *J. Electrochem. Soc.*, 2007, **154**, C515.

13. H. Asteman and M. Spiegel, 'Investigation of the HCl (g) attack on pre-oxidized pure Fe, Cr, Ni and commercial 304 steel at 400 °C,' *Corros. Sci.*,2007, **49**, 3626–3637.

14. C. Pettersson, J. Pettersson, H. Asteman, J.-E. Svensson, and L.-G. Johansson, 'KCl-induced high temperature corrosion of the austenitic Fe–Cr–Ni alloys 304L and Sanicro 28 at 600 °C," *Corros. Sci.*, 2006, **48**, 1368–1378.

15. H. J. Grabke, E. and Reese, and M. Spiegel, 'The effects of chlorides, hydrogen chloride, and sulfur dioxide in the oxidation of steels below deposits,' *Corros. Sci.*, 1995, **37**, 1023–1043.

16. Y. Y. Lee and M. J. Mcnallan, 'Ignition of Nickel in Environments Containing Oxygen and Chlorine,' *Metall. Mater. Trans. A*, 1987, **18**, 1099–1107.

17. S. Sroda and S. Tuurna, 'Laboratory scale tests on corrosion behavior of boiler materials in simulated combustion atmospheres (EU Project – OPTICORR),' *Mater. Corros.*, 2006, **57**, 244–251.

18. H. P. Nielsen, F. J. Frandsen, and K. Dam-Johansen, 'Lab-Scale Investigations of High-Temperature Corrosion Phenomena in Straw-Fired Boilers,' *Energy & Fuels*, 1999, **13**,1114–1121.

19. S. C. Van Lith, F. J. Frandsen, M. Montgomery, T. Vilhelmsen, and S. A. Jensen, 'Lab-scale Investigation of Deposit-induced Chlorine Corrosion of Superheater Materials under Simulated Biomass-firing Conditions. Part 1: Exposure at 560 °C,' *Energy & Fuels*, 2009, **59**, 3457–3468.

20. H. J. Grabke and D. B. Meadowcroft, 'A Working Party Report on Guidelines for Methods of Testing and Research in High Temperature Corrosion,' European Federation of Corrosion Publication Number 14, UK, 1995.

21. K. E. Coleman, N. J. Simms, P. J. Kilgallon, and J. E. Oakey, 'Corrosion in Biomass Combustion Systems,' *Mater. Sci. Forum*, 2009, **595–598**, 377–386.

22. K. Pantleon and M. Montgomery, 'Phase Identification and Internal Stress Analysis of Steamside Oxides on Plant Exposed Superheater Tubes,' *Metall. Mater. Trans. A*, 2012, **43A**, 1477–1486.

23. M. Montgomery, A. Karlsson, and O. H. Larsen, 'Field test corrosion experiments in Denmark with biomass fuels. Part 1: Straw-firing,' *Mater. Corros.*, 2002, **53**, 121–131.

24. M. Montgomery and A. Karlsson, 'In-situ corrosion investigation at Masnedø CHP plant -A straw-fired power plant,' *Mater. Corros.*, 1999, **584**, 579–584.

25. L. A. Hansen, H. P. Nielsen, F. J. Frandsen, K. Dam-Johansen, S. Hørlyck, and A. Karlsson, 'Influence of deposit formation on corrosion at a straw-fired boiler,' *Fuel Process. Technol.*, 2000, **64**, 189–209.

26. L. Boonsongsup, K. Iisa, and W. J. Frederick, 'Kinetics of the Sulfation of NaCl at Combustion Conditions,' *Ind. Eng. Chem. Res.*, 1997, **5885**, 4212–4216.

27. K. Iisa, Y. Lu, and K. Salmenoja, 'Sulfation of Potassium Chloride at Combustion Conditions,' *Energy & Fuels*, 1999, **13**, 1184–1190.

28. H. J. Zahs, A., Spiegel, M., Grabke, ‘The influence of alloying elements on the chlorine-induced high temperature corrosion of Fe-Cr alloys in oxidizing atmospheres,’ *Mater. Corros.*, 1999, **50**, 561–578.

29. R. A. Antunes and M. C. L. de Oliveira, ‘Corrosion in biomass combustion: A materials selection analysis and its interaction with corrosion mechanisms and mitigation strategies,’ *Corros. Sci.*, 2013, **76**, 6–26.

30. J. Pettersson, J. E. Svensson, and L. G. Johansson, ‘Alkali Induced Corrosion of 304-Type Austenitic Stainless Steel at 600 °C; Comparison between KCl, K_2CO_3 and K_2SO_4,’ *Mater. Sci. Forum*, 2008, **595–598**, 367–375.

31. N. Folkeson, T. Jonsson, M. Halvarsson, L.-G. Johansson, and J.-E. Svensson, ‘The influence of small amounts of KCl(s) on the high temperature corrosion of a Fe-2.25Cr-1Mo steel at 400 and 500°C,’ *Mater. Corros.*, 2011, **62**, 606–615.

32. R. Bender and M. Schütze, ‘The role of alloying elements in commercial alloys for corrosion resistance in oxidizing-chloridizing atmospheres Part I : Literature evaluation and thermodynamic calculations on phase stabilities,’ *Mater. Corros.*, 2003, **586**, 567–586.

33. H. . Spiegel, M., Zahs, A., Grabke, ‘Fundamental aspects of chlorine induced corrosion in power plants,’ *Mater. High Temp.*, 2003, **20**, 153–159.

34. R. Bender and M. Schütze, ‘The role of alloying elements in commercial alloys for corrosion resistance in oxidizing-chloridizing atmospheres. Part II: Experimental investigations,’ *Mater. Corros.*, 2003, **54**, 652–686.

35. H. Latreche, S. Doublet, and M. Schütze, ‘Development of Corrosion Assessment Diagrams for High Temperature Chlorine Corrosion Part II: Development of ‘Dynamic’ Quasi-stability Diagrams,’ *Oxid. Met.*, 2009, **72**, 31–65.

Figures

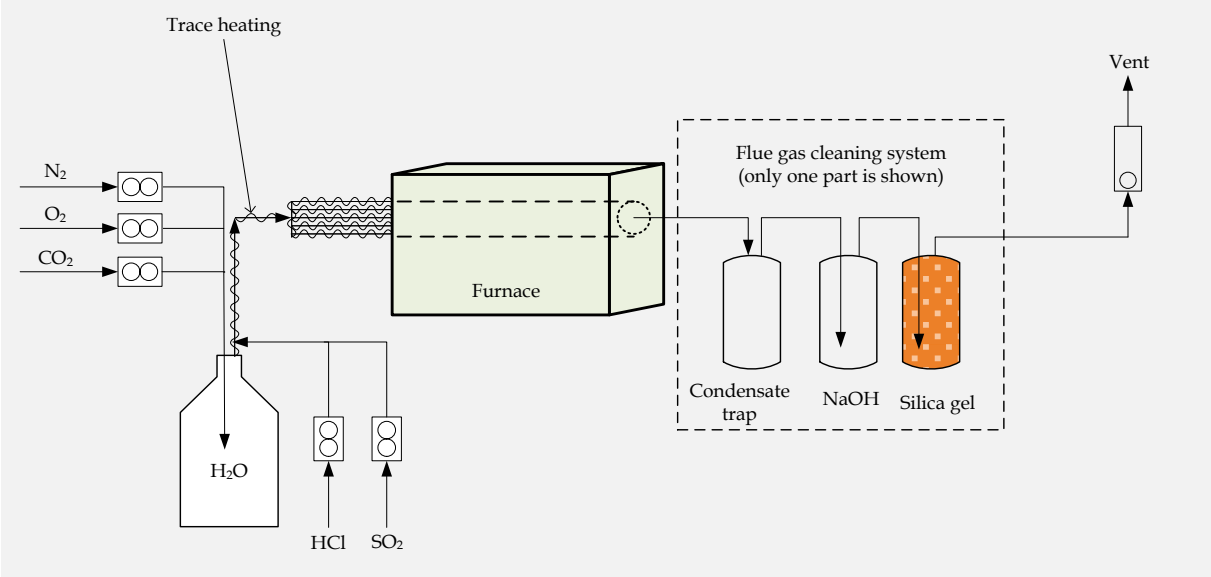

Figure 1 A schematic representation of the corrosion test rig used for the high temperature exposure. A single part of the cleaning system is shown for clarity.

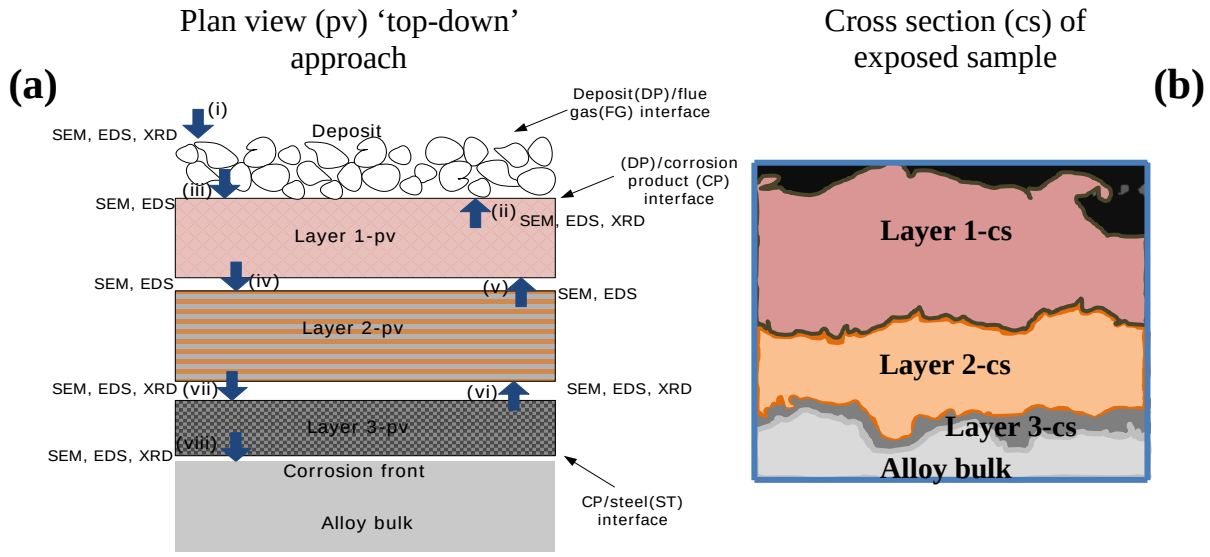

Figure 2 Schematic representation of the plan view 'top-down' characterization approach (a) related to the corresponding cross section (b) of the exposed sample. The location of the various layers of corrosion product (1 to 3) is indicated. The arrows in (a) show the directions from which investigations were carried out. Characterization techniques used at each investigated position (i to viii) are shown. (DP = Deposit, FG = Flue gas, CP = Corrosion product, ST = Steel).

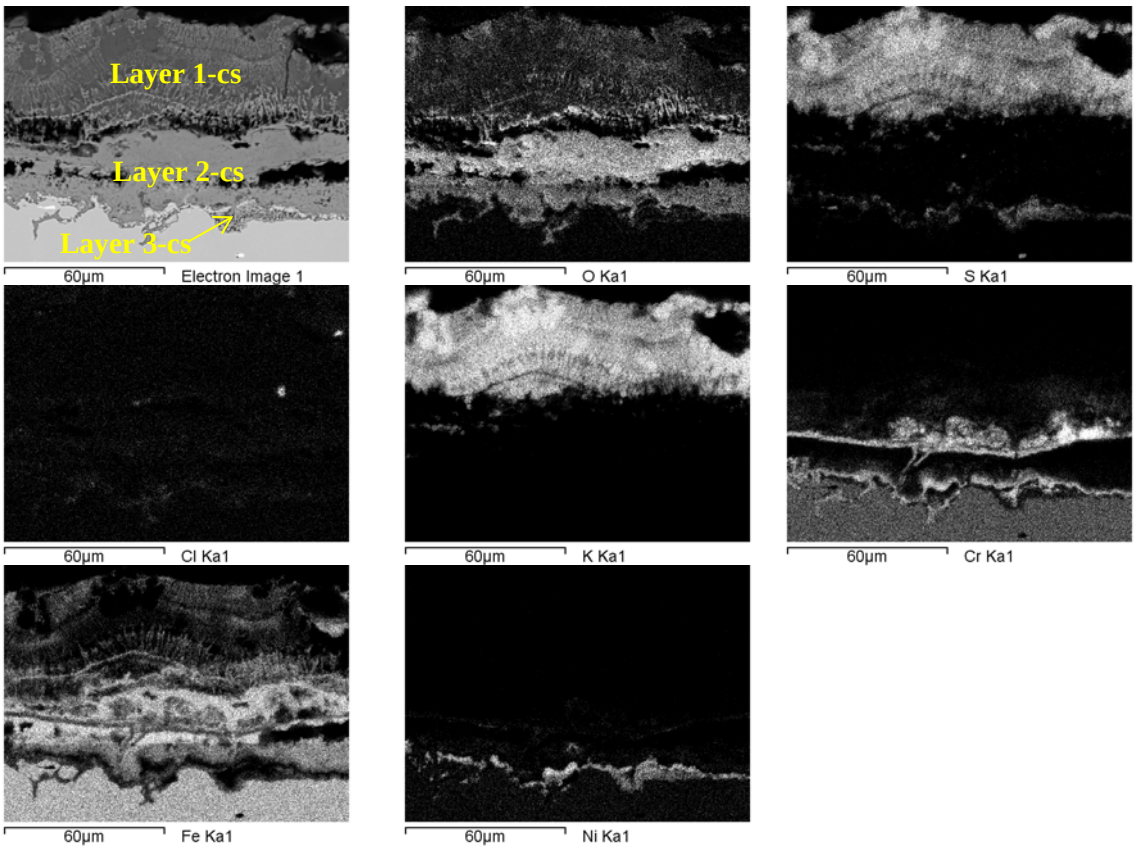

Figure 3 Elemental distribution across the cross section of an exposed sample obtained by EDS mapping.

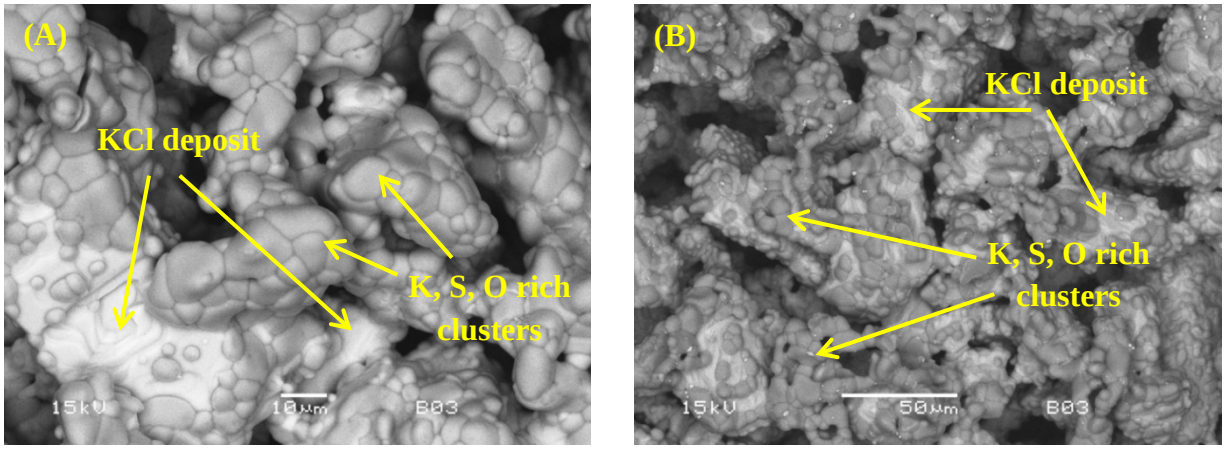

Figure 4 SEM Backscattered Electron (BSE) micrograph showing the morphology of the initial deposit particles at (a) the flue gas/deposit interface and (b) at the deposit/corrosion product interfaces. These positions correspond to the locations indicated in Fig. 2a as (i) and (ii), respectively.

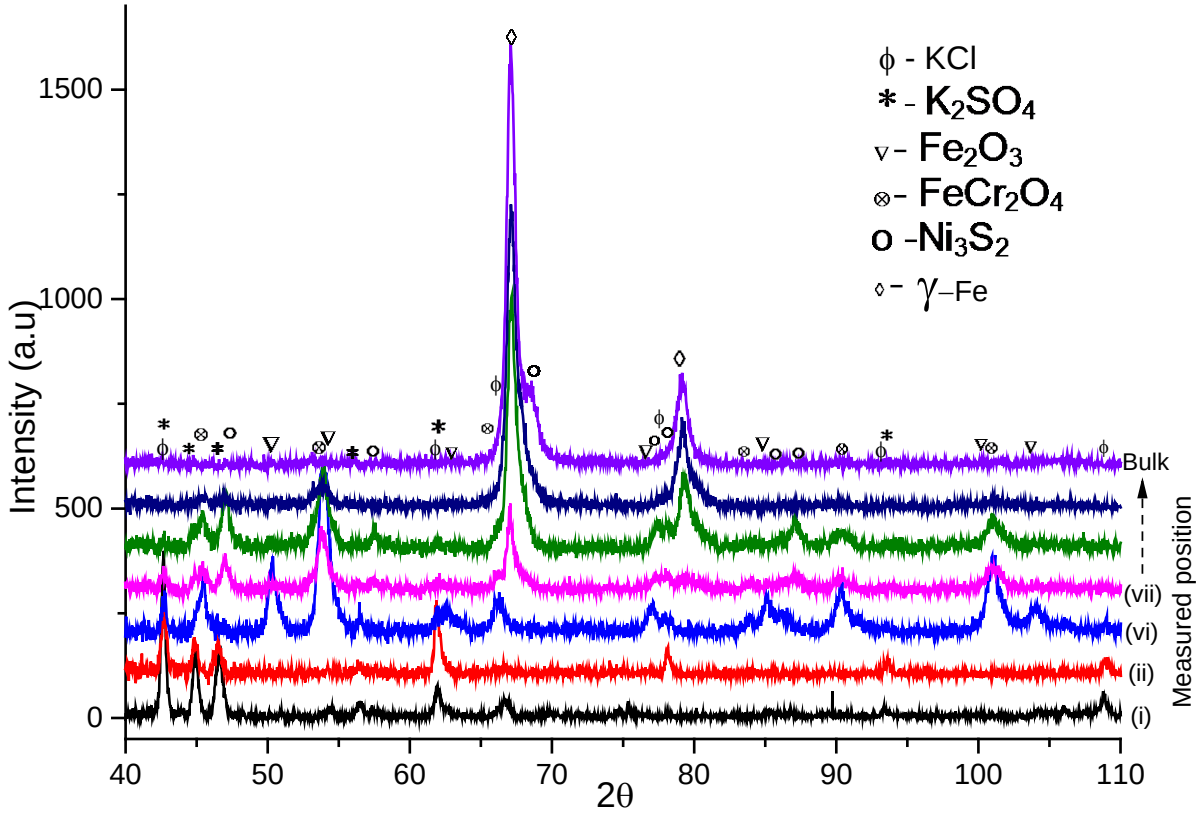

Figure 5 X-Ray diffractograms showing the prevalent crystalline chemical phases from plan view characterization of the corrosion products at various depths. The corresponding measurement positions indicated on the right horizontal axis correspond to the positions indicated in Fig. 2.

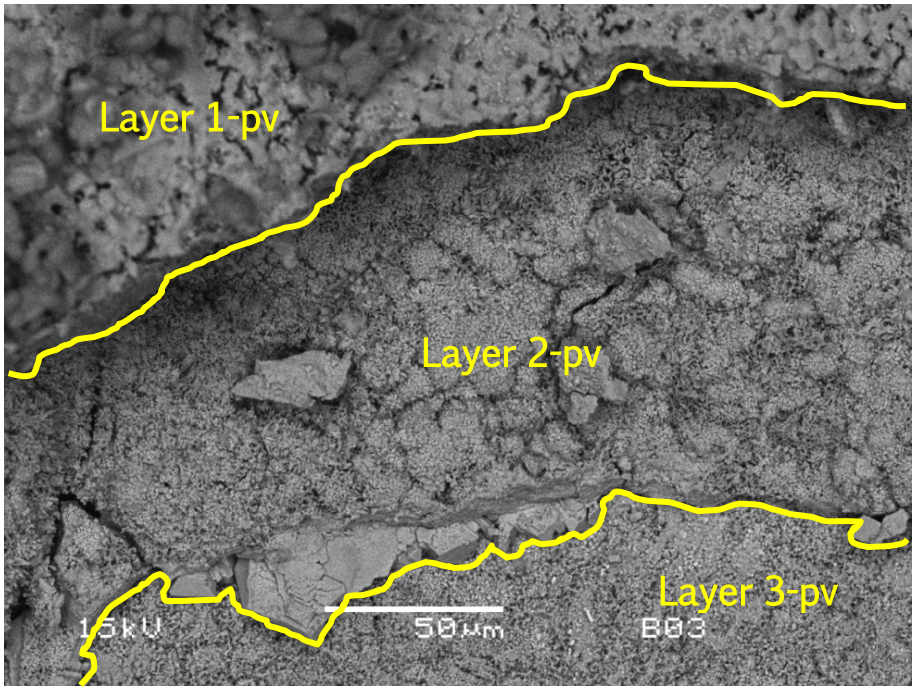

Figure 6 SEM BSE micrograph showing a plan view of the corrosion product (viewed from the location indicated as (iii) in Fig. 2a). Due to the fracture of the CP layers during removal, it was possible to view all three layers of the CP.

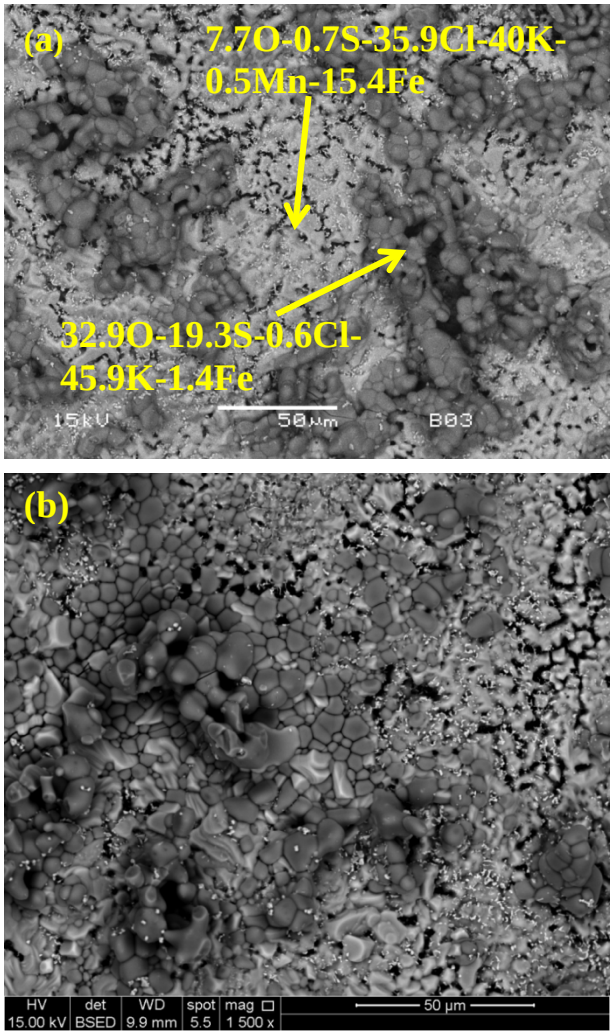

Figure 7 SEM BSE micrograph showing the morphology of the first layer of corrosion product below the initial deposit (Layer 1-pv in Fig. 6). The micrographs (7a) and (7b) were obtained from the positions indicated as (iii) and (v) in Fig. 2a. Average chemical compositions (in wt.-%) obtained from EDS analysis are inserted in the micrograph.

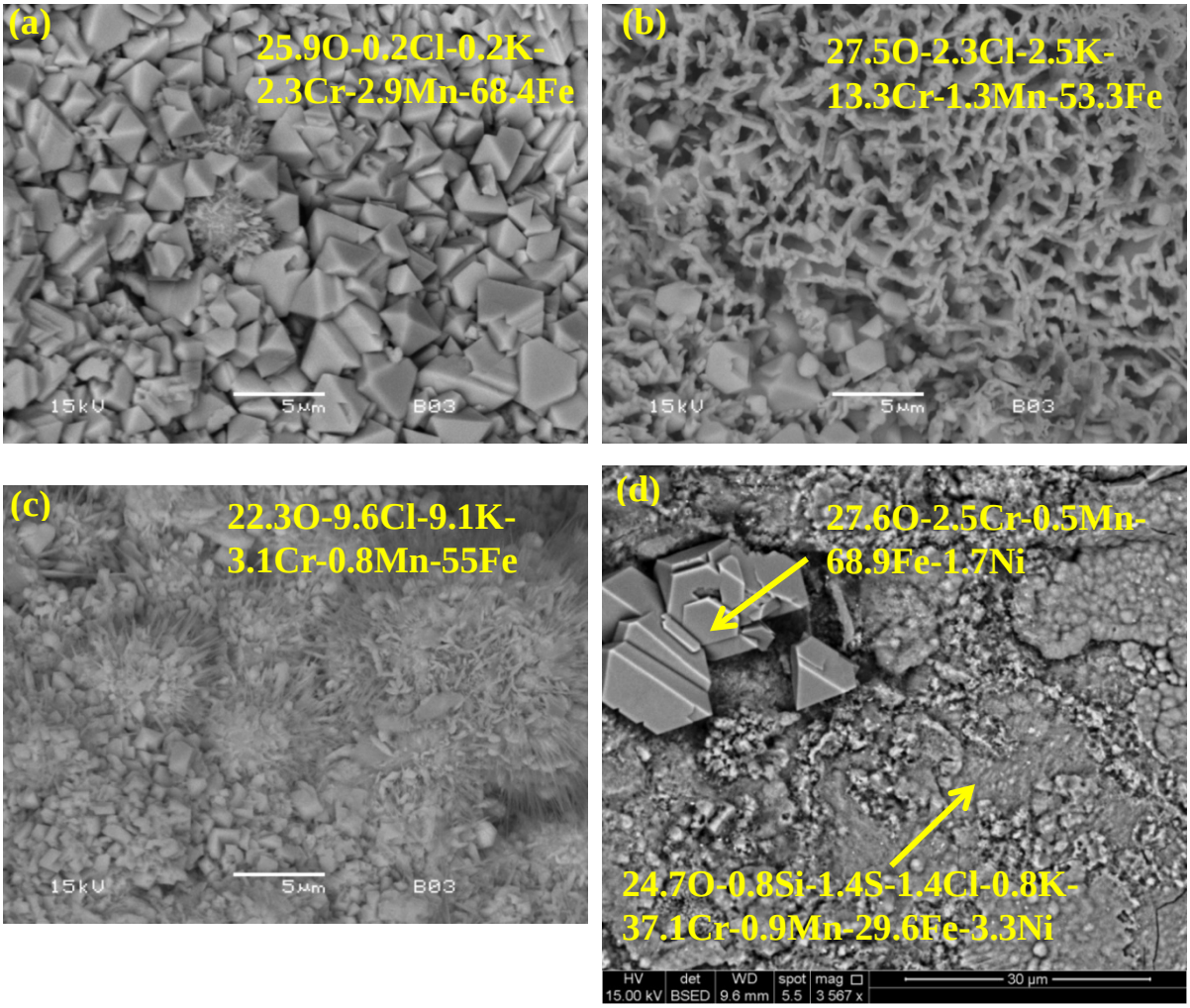

Figure 8 SEM BSE micrograph showing the morphology of Layer 2-pv of corrosion product, below the initial deposit. The micrographs (a), (b) and (c) were acquired from the position indicated as (iv) in Fig. 2a. The micrograph in (d) was acquired from position (vi) in Fig. 2a. Results of EDS analysis (in wt.-%) at various locations are inserted in the micrographs.

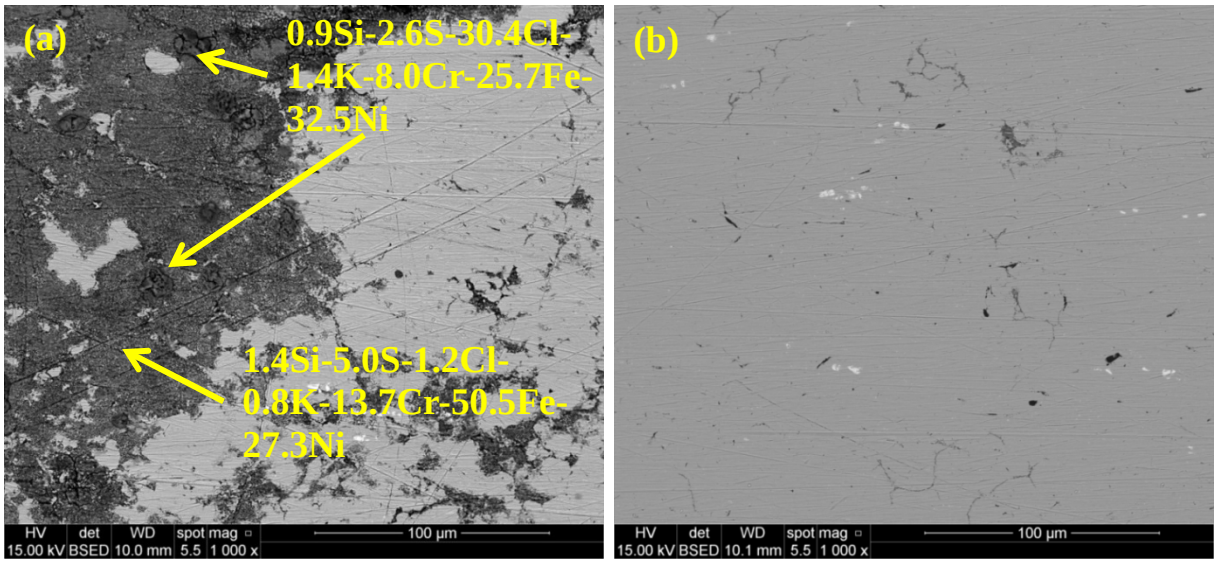

Figure 9 SEM BSE micrographs showing the morphology beneath the porous layer of corrosion product (i.e. beneath Layer 3-pv). (a) refers to position (vii) in Fig. 2a, (b) is close to the corrosion front. Average chemical compositions of the melt phases (dark protrusions in Fig. 9a) and the porous regions (in wt.-%) obtained from EDS analysis are shown on the micrograph.

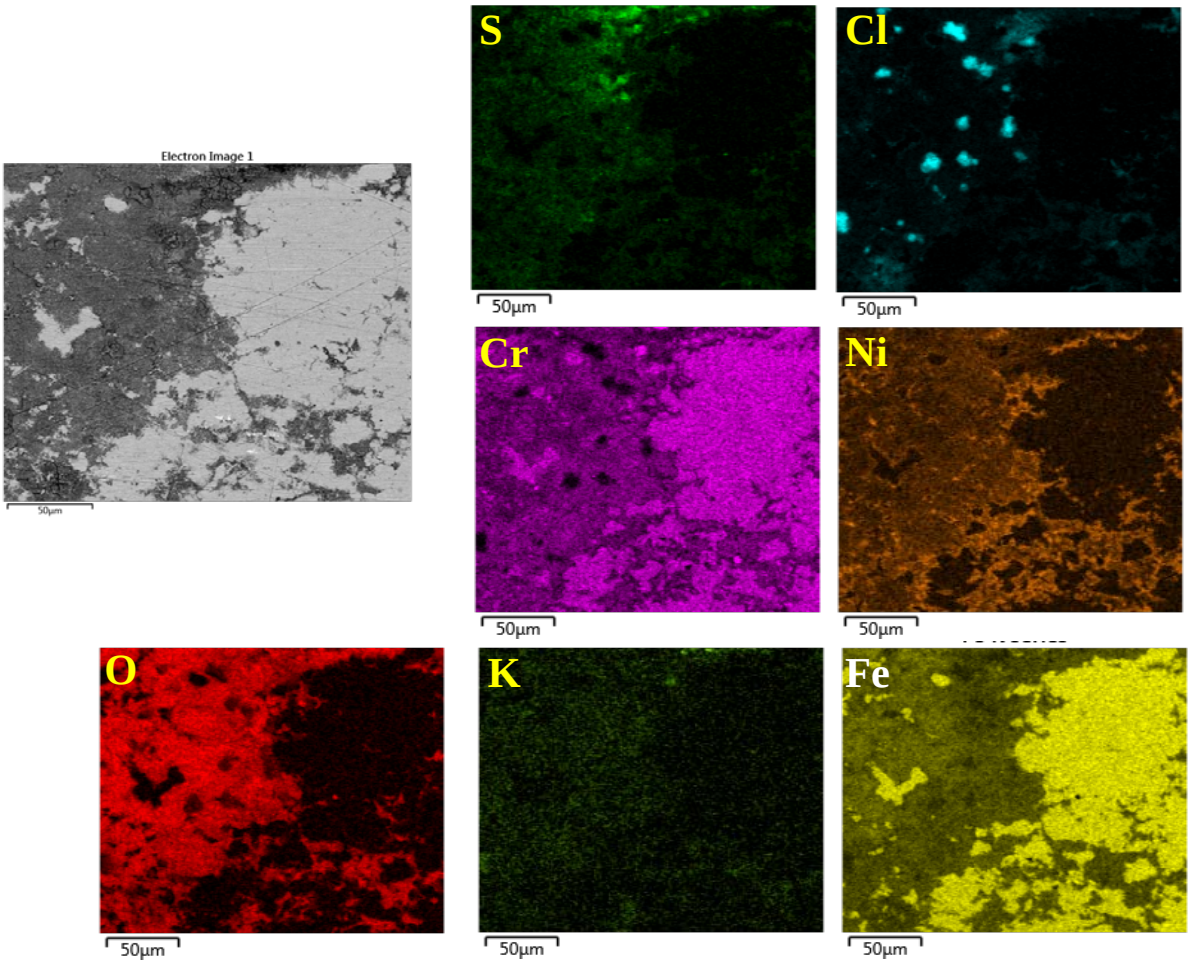

Figure 10 EDS elemental maps of the porous layer below Layer 3-pv of corrosion product.

The location corresponds to the one shown in Fig. 9a.